Electronic Supplementary Material (ESI) for Chemical Science.

Supporting Information

A compatible anode/succinonitrile-based electrolyte interface in all-solid-state Na–CO_2 batteries

*Yong Lu, Yichao Cai, Qiu Zhang, Luojia Liu, Zhiqiang Niu, and Jun Chen**

Key Laboratory of Advanced Energy Materials Chemistry (Ministry of Education), Renewable Energy Conversion and Storage Center, College of Chemistry, Nankai University, Tianjin 300071, China

*Correspondence: chenabc@nankai.edu.cn

Table of Contents

Computational Details

DFT calculations

The first-principles density functional theory (DFT) calculations were carried out with Gaussian 09W program package for single Na^+, FEC, and FEC-Na^+, under B3LYP level of theory with the basis set 6-31+G(d,p).[1–3] The vibrational frequency calculations were performed along with optimization for each entity to further confirm the stability of the structures. The LUMO and HOMO plots were obtained by using GaussView 3.0.

AIMD calculations

The *ab initio* molecular dynamics (AIMD) on Na (110) surface were performed using Vienna Ab initio Simulation Package (VASP) with the generalized gradient approximation (GGA) and the Perdew-Burke-Eznerhof (PBE) functional (GGA-PBE) to describe the exchange-correlation energy of electrons.[4–7] The projector-augmented wave method (PAW) was used to treat the interaction between the atomic cores and electrons.[8,9] The reciprocal space was covered by a 2×2×1 Monkhorst-Pack k-point grid with Γ point and a cutoff of 400 eV were used for the investigated surface slab cell (~13 Å×18 Å×35 Å).[10] In this work, AIMD simulation was performed to observe the decomposition of FEC and FEC-Na^+ at 2000 K using the canonical (NVT) ensemble for 1 ps with 1 fs time steps.

Experimental Section

Modification of Na metal

The Na metal was first cured into circles (8 mm in diameter) and then treated by adding 1 M $NaClO_4$/FEC (20 μL) on its one side. After treatment for 1, 5, or 30 s, the residual $NaClO_4$/FEC was wiped completely by filter paper to obtain the modified Na metal, which can be used as anodes directly.

Preparation of solid-state electrolyte

The all-solid-state electrolyte consisting of succinonitrile (SN), poly(vinylidene fluoride-*co*-hexafluoropropylene) (PVDF-HFP), and $NaClO_4$ was prepared as follows. 0.8 g PVDF-HFP (Sigma-Aldrich) with an average molecular weight of 455,000 was first added into 8 mL anhydrous acetone. The mixture was stirred at 50 ℃ for 2 h until PVDF-HFP was dissolved completely. Then, 0.0764 g $NaClO_4$ was added to the solution and the solution was stirred for another 30 mins. After that, 1 g SN (the molar ratio of SN to $NaClO_4$ is fixed as 20:1) was added to the solution and stirred for another 10 mins to form homogeneous solution. Finally, the solid-state electrolyte (SSE) was obtained by casting on a clean glass plate with a doctor blade and followed by dried at 25 ℃ for 10 h in an Ar-filled glove box. Other SSEs with different ratio of PVDF-HFP can be prepared by adjusting the amounts of added PVDF-HFP. The SSEs with different thickness can be obtained by adjusting the depth of doctor blade. All the procedures to prepare SSEs were conducted in an Ar-filled glove box.

Preparation of integrated SSE/MWCNTs cathode

The integrated SSE/MWCNTs cathode can be obtained by two main steps, including the preparation of MWCNTs cathode and coating with SSE. Prior to use, the multi-walled carbon nanotubes (MWCNTs, Cnano Technology Ltd.) were functionalized by acidic treatment (refluxing in the mixture of HNO_3 and H_2SO_4 at 110 ℃ for 6 h), as described in our previous work.[11] First, 10 mg functionalized MWCNTs was dispersed in ethanol (100 mL) by ultrasonication for 2 h. The MWCNTs suspension

was sprayed on carbon paper (10×10 cm^2, TORAY, Japan) at 100 ℃. The obtained MWCNTs cathode was then dried at 110 ℃ for 4 h. Finally, the homogeneous SN/PVDF-HFP/$NaClO_4$ solution was cased onto the MWCNTs cathode and then dried at 25 ℃ for 10 h in an Ar-filled glove box to form the integrated SSE/MWCNTs cathode.

Preparation of $Na_3V_2(PO_4)_3$ sample

The $Na_3V_2(PO_4)_3$ sample was prepared by a sol-gel approach. The detailed synthetic process can be found in our previous work.[12]

Materials characterization

The elemental information and the surface chemical composition were measured by X-ray photoelectron spectroscopy (XPS, PerkinElmer PHI 1600 ESCA). The morphologies and elemental mapping were confirmed by field-emission scanning electron microscopy (SEM, JEOL JSM7500F) and transmission electron microscopy (TEM, FEI Talos F200x G2). AFM topography image and Young's modulus mapping were collected with Scan Asyst Mode and Peak Force QNM mode, respectively (Dimension Icon, Bruker). XRD patterns were obtained by Rigaku MiniFlex600 (CuKα radiation). IR spectra were achieved by Fourier transform infrared spectroscopy (Bruker Tensor II Sample Compartment RT-DLaTGS). The thermal stability of the SSE was measured by thermogravimetric analyzer (NETZSCH, STA 449F3). The melting point of the SSE was confirmed via X-4B Microscope Melting Point Apparatus (SHRY Scientific Instruments Co., Ltd). The tensile test of different SSEs was conducted on a Dynamic Mechanical Analyzer (TA DMA Q800). The Raman spectra are recorded with a Thermo-Fisher Scientific (excitation wavelength, 532 nm).

Electrochemical measurement

The all-solid-state Na–CO_2 batteries were tested by using CR2032 coin-type cells with pristine or modified Na metal anode and integrated SSE/MWCNTs cathode. The mass loading of MWCNTs in

the cathode is about 0.1 mg cm^{-2}. The batteries were assembled in an Ar-filled glove box and the modified side of Na metal was contacted with the integrated cathode. Then the batteries were placed in 200 mL glass vessel, which was filled with pure CO_2 by double-rowed pipe for five times. Prior to test, the batteries rest for 6 h. The galvanostatic discharge/charge measurements at different current densities were performed with Land CT2001A battery instrument at room temperature. The capacities and current densities are based on the mass of MWCNTs. Linear sweep voltammetry (LSV) in the voltage range of 1.0–5.3 V and electrochemical impedance spectroscopy (EIS) tests in the frequency range of 100k–0.1 Hz (or 100k–100 Hz) with the amplitude of 5 mV were conducted by using CHI 660E electrochemical workstation (ChenHua, Shanghai). The ionic conductivity of SSEs can be obtained by EIS, as described in the previous work.[13] The EIS tests at different temperatures were performed in an incubator.

Analogously, the all-solid-state Na|$Na_3V_2(PO_4)_3$ batteries are composed of Na metal (pristine or modified) anode and integrated SSE/$Na_3V_2(PO_4)_3$ cathode. The $Na_3V_2(PO_4)_3$ cathode consists of prepared $Na_3V_2(PO_4)_3$ sample (70 wt%), conductive carbon materials (Ketjen black, 20 wt%), and polyvinylidene fluoride (PVdF) binder (10 wt%). The current collector is Al foil. The all-solid-state $Na_3V_2(PO_4)_3$|$Na_3V_2(PO_4)_3$ symmetric batteries were fabricated by using integrated SSE/$Na_3V_2(PO_4)_3$ as the anode and cathode. The charge/discharge capacities are calculated based on the total mass of the synthesized sample ($Na_3V_2(PO_4)_3$ and MWCNTs).

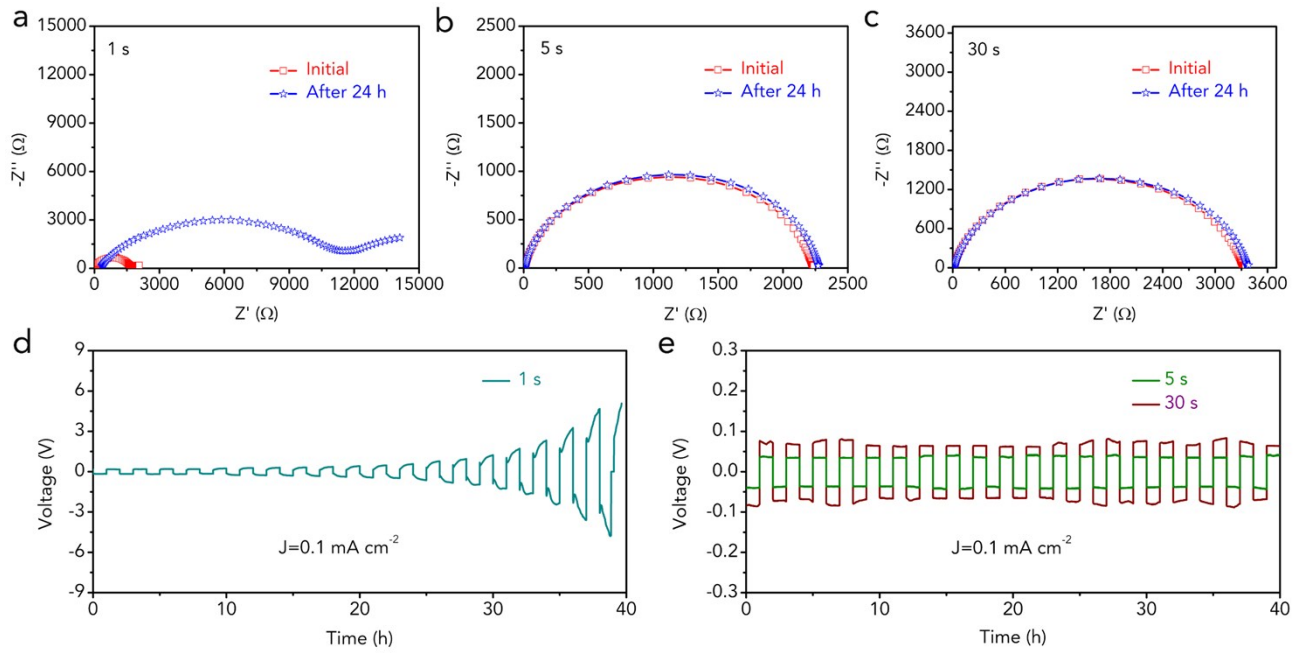

Figure S1. Optimization of reaction time between Na metal and 1M $NaClO_4$/FEC. EIS of the symmetric cells (initial and after 24 h) with different modified Na anodes: (a) 1 s, (b) 5s, and (c) 30 s. Voltage profiles of the symmetric cells with different modified Na anodes: (d) 1 s, (e) 5s and 30 s.

When the reaction time of Na metal and 1M $NaClO_4$/FEC is too short (1 s), the resistance of the corresponding symmetric cells increased remarkably after rest for 24 h (Figure S1a) and overpotential gradually became very large (Figure S1d), indicating integrated and compact NaF-rich interphase could not form on the surface of Na metal owing to the short reaction time. In contrast, when the reaction time is extended to 5 s, the stable resistance (Figure S1b) and voltage profiles (Figure S1e) demonstrate the effective protection of the NaF-rich interphase. However, when the reaction time is too long (30 s), the integrated NaF-rich interphase could also generate but the resistance (Figure S1c) and overpotential (Figure S1e) is larger than that with 5 s. Therefore, we select 5 s as the optimized reaction time for further studies.

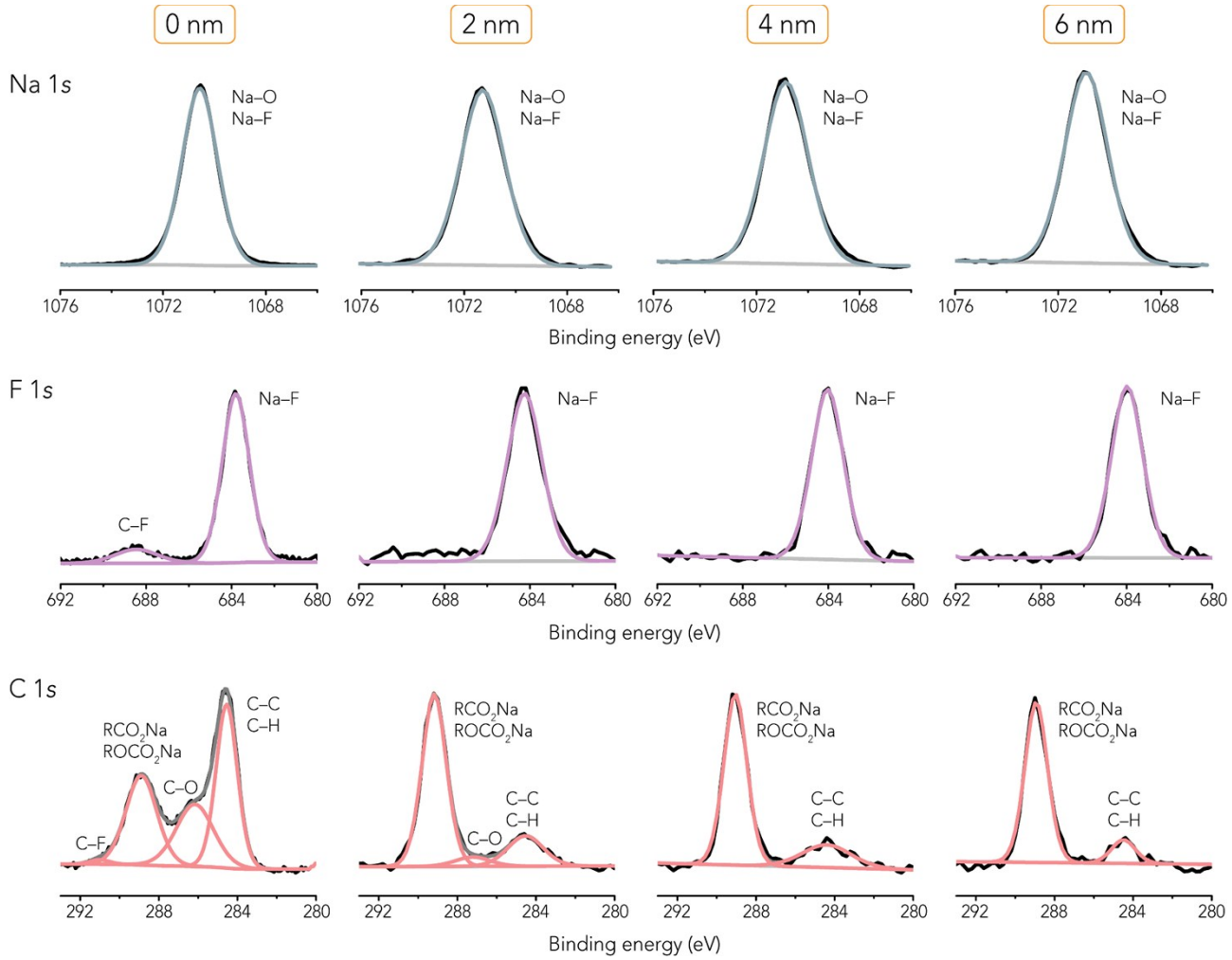

Figure S2. High-resolution XPS spectra of Na 1s, F 1s, and C 1s of the in situ formed NaF-rich interphase at different depth (0, 2, 4, and 6 nm).

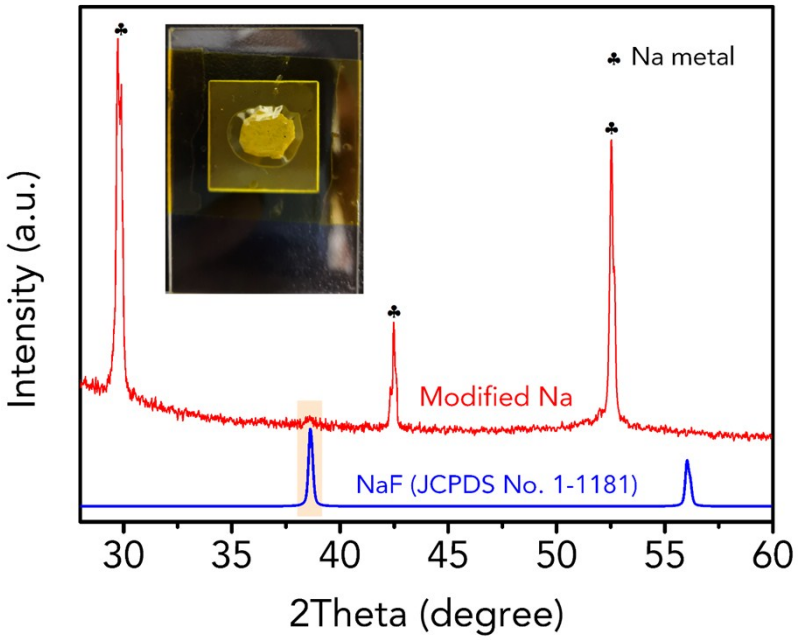

Figure S3. XRD pattern of the Na metal modified by 1M $NaClO_4$/FEC. During XRD test (condition: from 28^0 to 60^0 at a scan rate of 4^0/min), the sample was sealed by Kepton film (the inset shows the optical photograph).

Note that the signals originated from Na metal are much stronger than that of NaF, which can be attributed to the fact that the generated NaF-rich interphase is too thin.

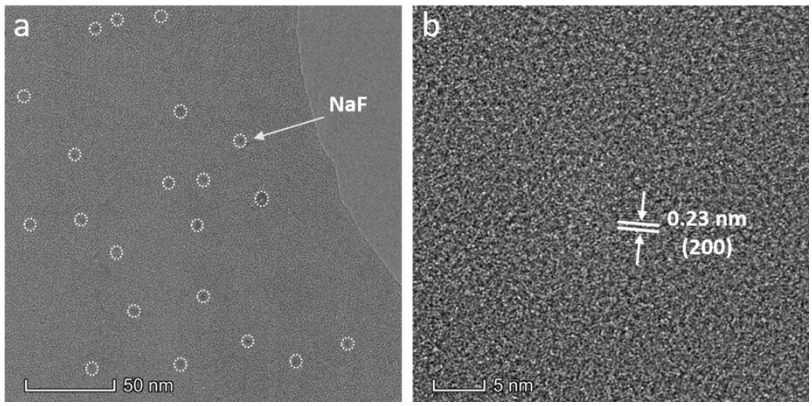

Figure S4. TEM images at (a) low and (b) high magnifications of the NaF-rich interphase. The crystal face (200) of NaF has been marked in (b).

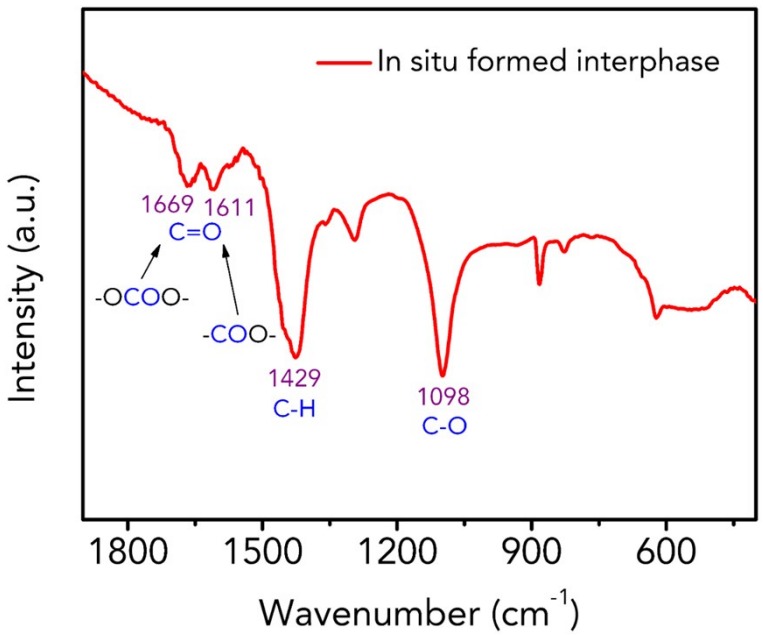

Figure S5. IR spectrum (ATR mode) of the in situ formed interphase on the surface of Na metal.

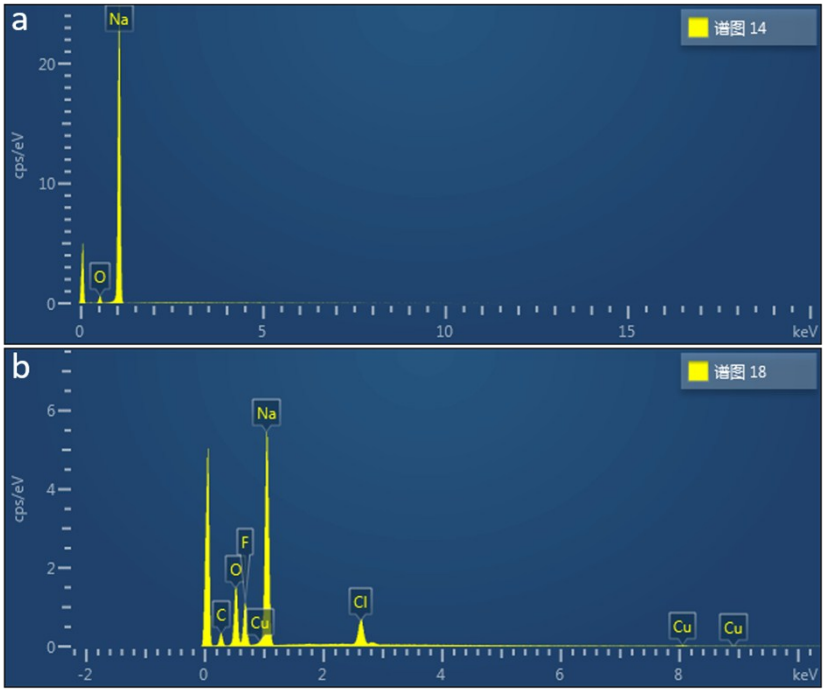

Figure S6. Energy dispersive X-ray spectroscopy of bare Na and modified Na. The content of O atom in bare Na is only 5.72 at% (Na atom: 94.28 at%), indicating that almost all the C, O, and F sources in the modified Na are only from the liquid reagent (1M $NaClO_4$/FEC).

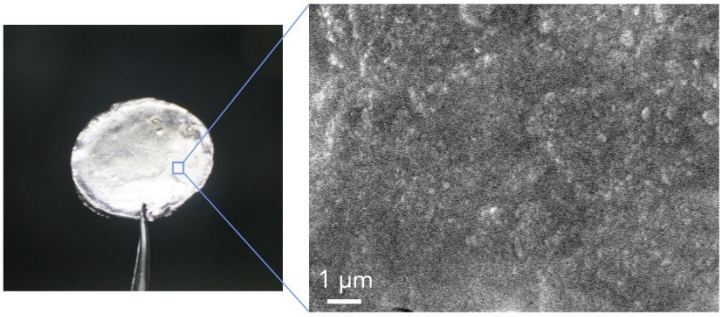

Figure S7. Optical photograph and SEM image of pristine Na metal.

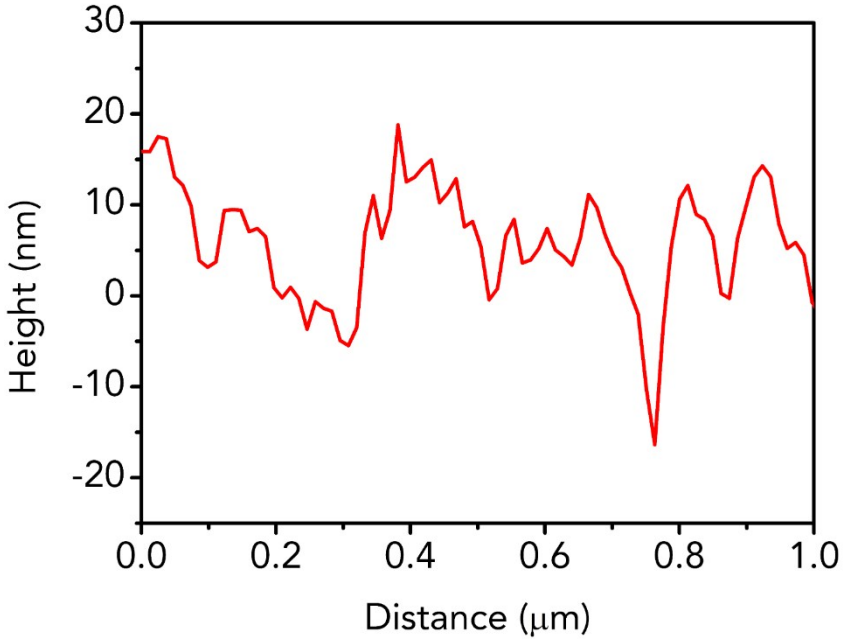

Figure S8. AFM roughness of the NaF-rich interphase on the surface of modified Na metal.

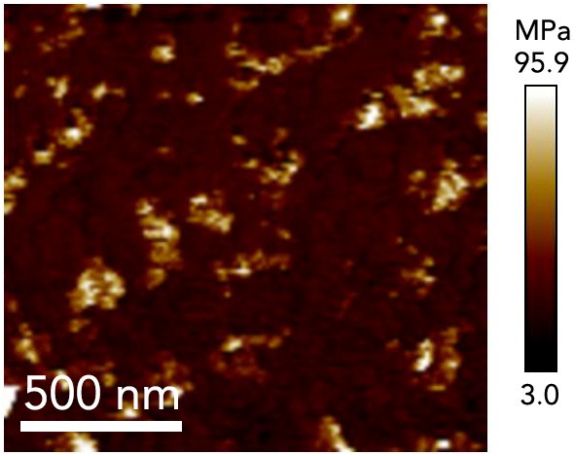

Figure S9. Young's modulus mapping of the NaF-rich interphase on the surface of modified Na metal.

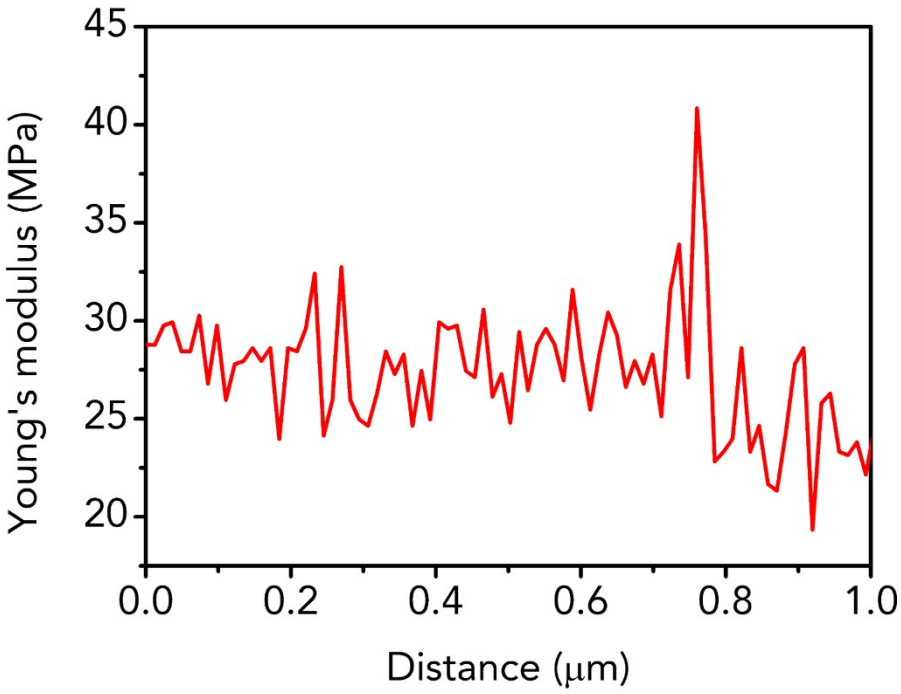

Figure S10. AFM Young's modulus of the NaF-rich interphase on the surface of modified Na metal.

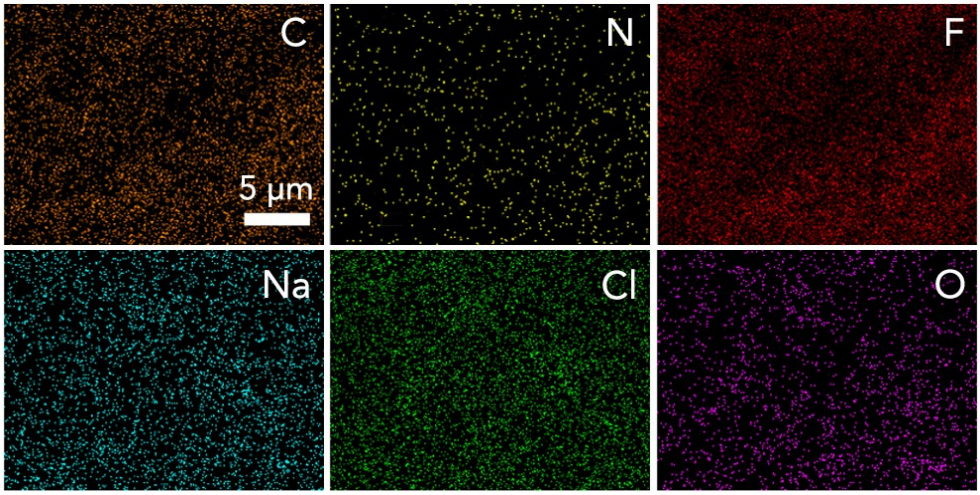

Figure S11. SEM elemental mappings (C, N, F, Na, Cl, O) of the obtained SN-based SSE.

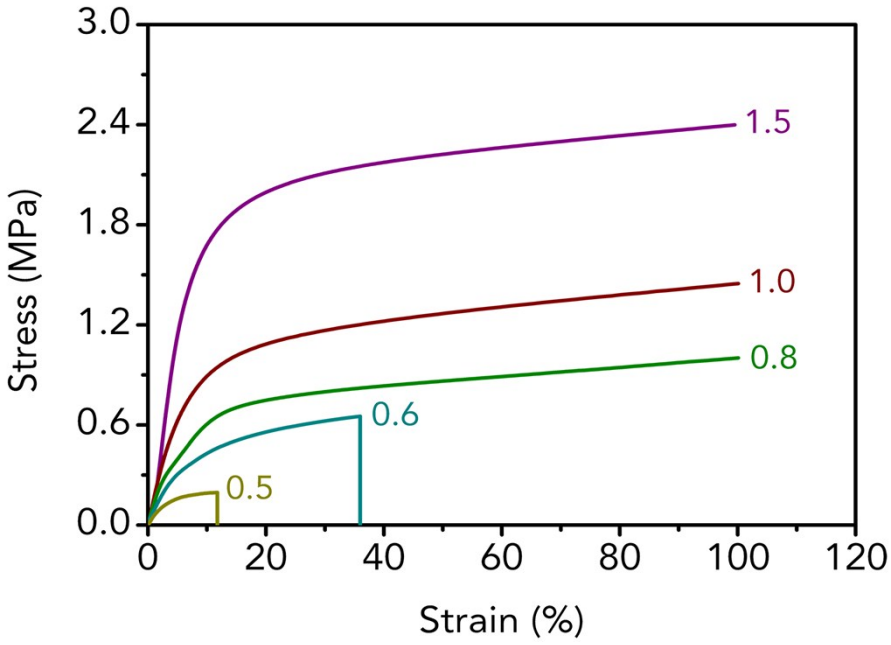

Figure S12. Stress-strain curves at a force speed of 0.01 N min^{-1} of the SN-based SSE with different contents of PVDF-HFP.

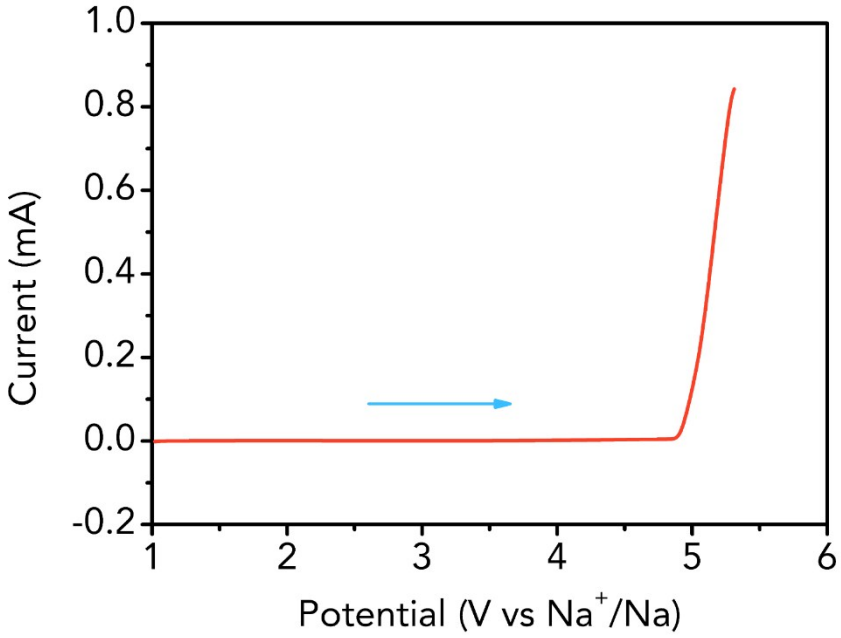

Figure S13. LSV of the obtained SN-based SSE in the voltage range of 1.0–5.3 V at a scan rate of 1 mV s^{-1}. The anodic decomposition potential of the SSE is 4.86 V (vs. Na^+/Na).

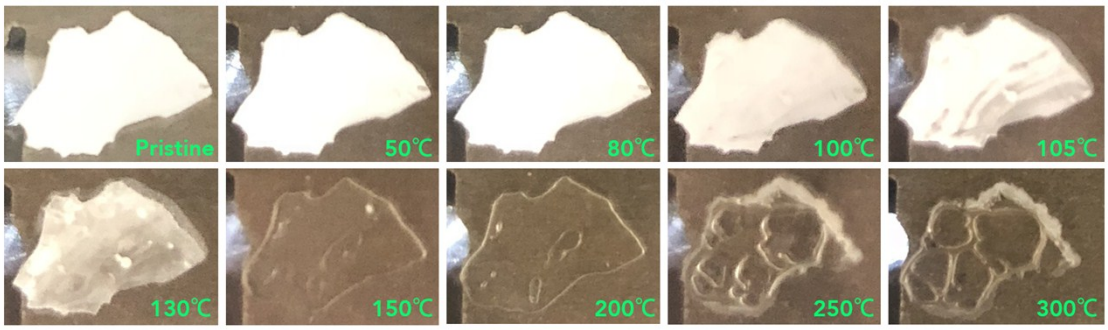

Figure S14. Optical photographs of the obtained SN-based SSE at different temperatures. The test was conducted on a microscope melting point apparatus. The results reveal that the SSE started to melt at about 105 ℃.

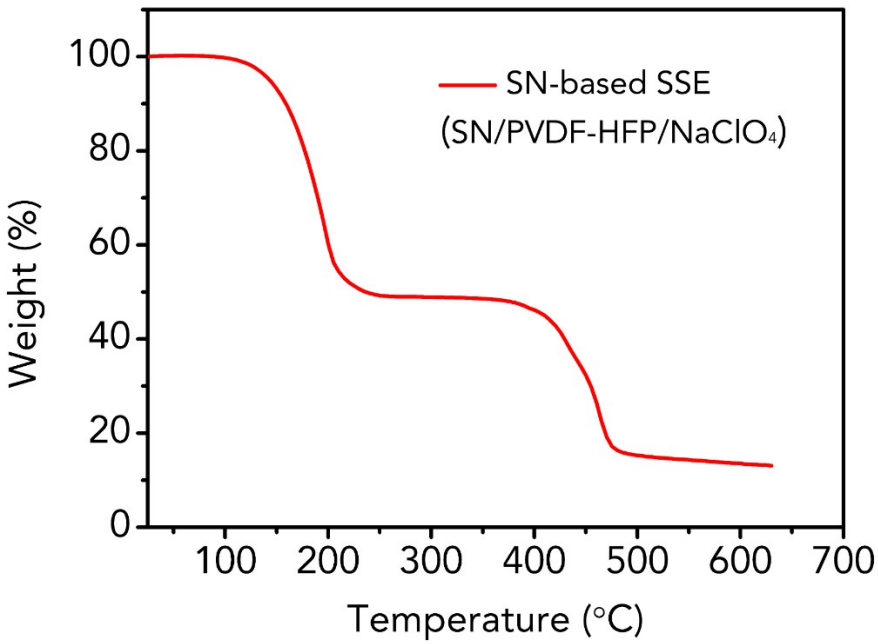

Figure S15. TG curve of the obtained SN-based SSE in the temperature range of 25–630 ℃ at a heat speed of 5 ℃ min^{-1} under Ar atmosphere.

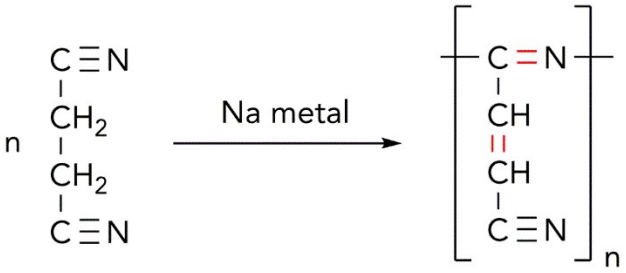

Figure S16. Proposed possible mechanisms for the polymerization of SN catalyzed by Na meal.[14]

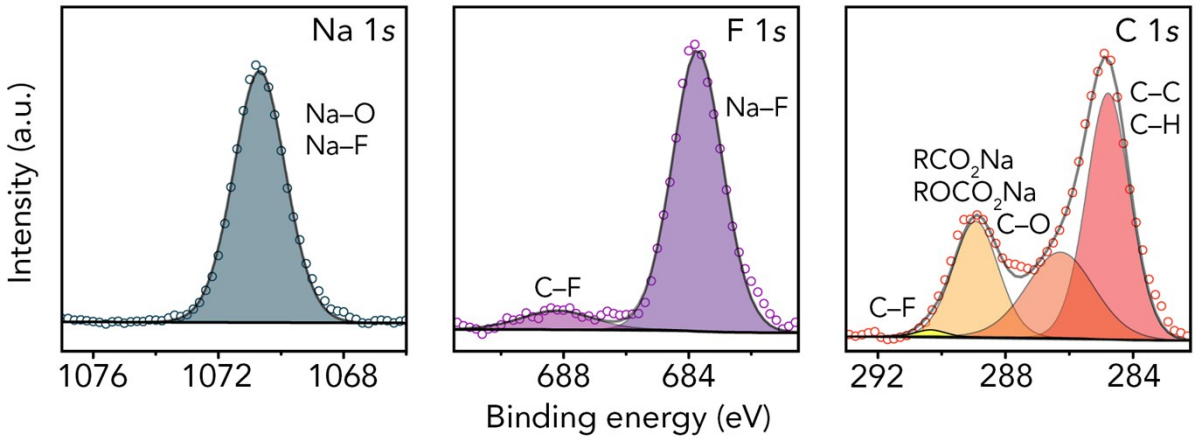

Figure S17. High-resolution XPS spectra of Na 1s, F 1s, and C 1s of the modified Na in symmetric cells after cycles (4000 h).

The binding energies of these elements are summarized as follows. (1) Na 1s: Na–O/Na–F (1070.7 eV); (2) F 1s: Na–F (683.7 eV), C–F (688.2 eV); and (3) C 1s: C–C/C–H (284.7 eV), C–O (286.3 eV), RCOONa/ROCOONa (288.9 eV), C–F (290.5 eV). The binding energies of each bonds of the modified Na after cycling for 4000 h are similar to that at initial state (Fig. 2a), demonstrating the high stability of the generated NaF-rich interphase on the surface of modified Na metal.

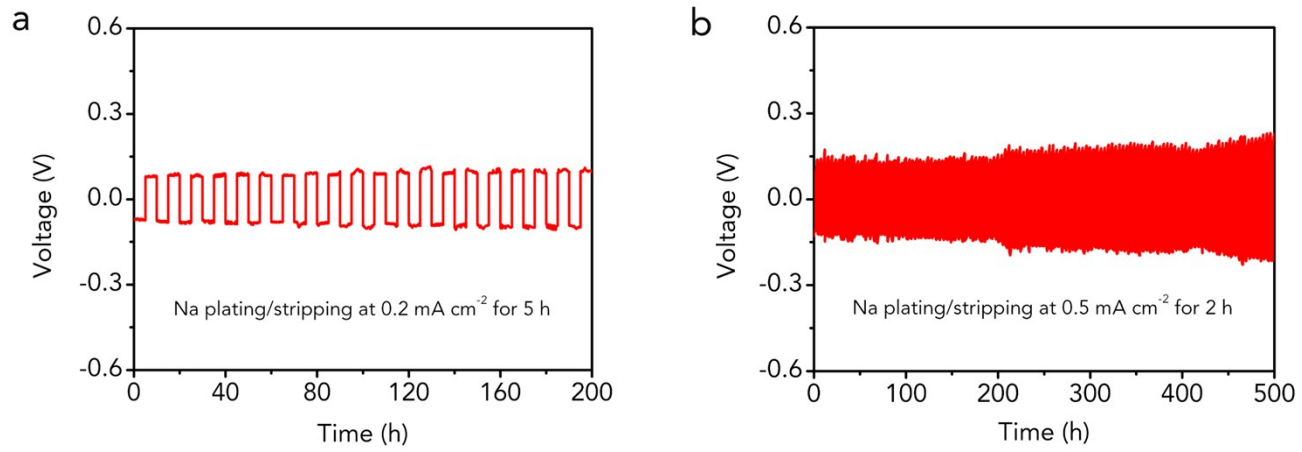

Figure S18. Electrochemical performance of M-Na|M-Na symmetric cells at higher current densities (a) 0.2 mA cm^{-2} and (b) 0.5 mA cm^{-2} for higher capacities (1 mA h cm^{-2}).

When the current densities are 0.2 and 0.5 mA cm^{-2}, the average overpotentials of symmetric cells (for 1 mA h cm^{-2}) are about 160 and 300 mV, respectively. Moreover, the symmetric cells under different current densities exhibit stable cycling performance, demonstrating that the modified Na metal could be used as a practical anode.

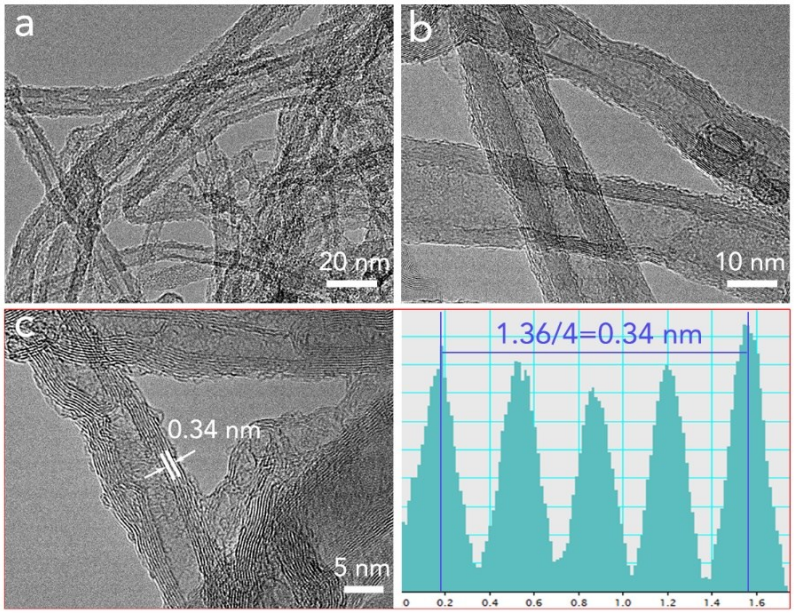

Figure S19. TEM images at low and high magnifications of the used MWCNTs in the cathode.

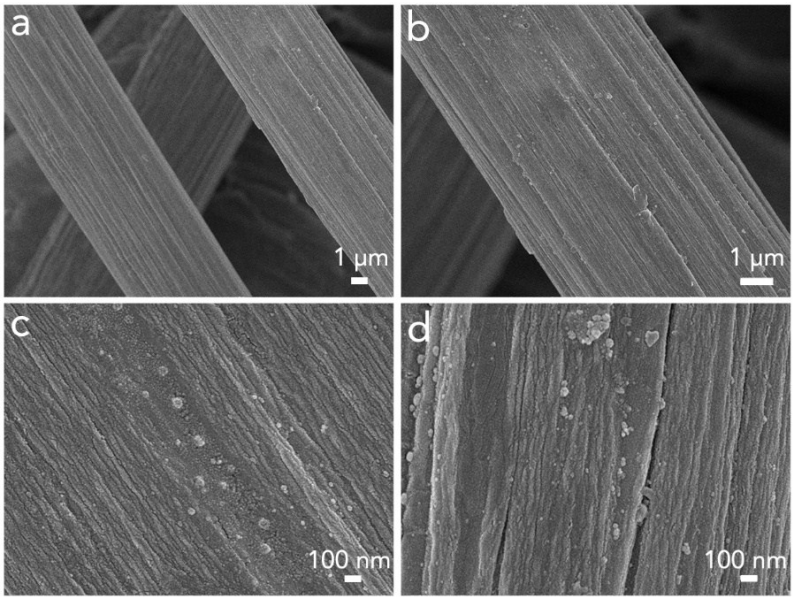

Figure S20. SEM images at low and high magnifications of the used carbon paper current collector in the cathode.

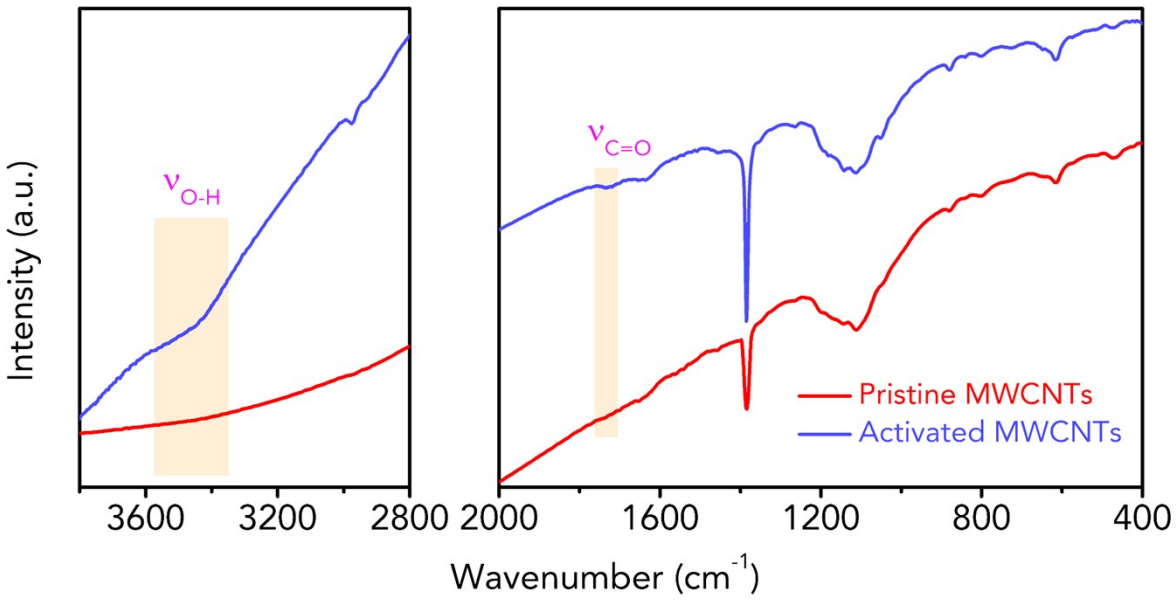

Figure S21. IR spectra of pristine and activated MWCNTs.

After pristine MWCNTs were activated by acidic treatment, the stretching vibrations of C=O and O–H emerged in the IR spectrum, implying the introduction of –COOH and –OH functional groups on MWCNTs after activation.

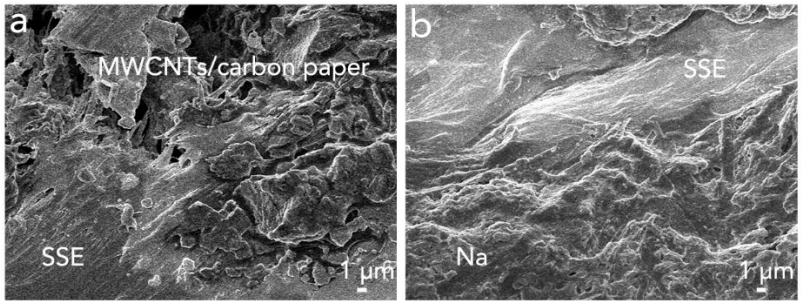

Figure S22. High-resolution SEM images of the interface between (a) SSE and MWCNTs in cathode, (b) Na anode and integrated cathode.

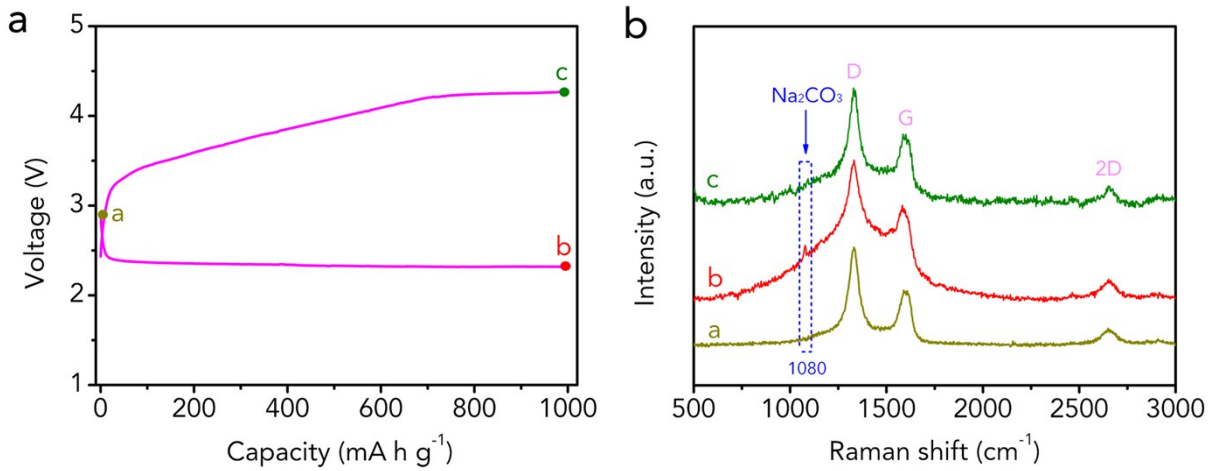

Figure S23. Ex situ Raman spectra to reveal the reaction mechanism of the all-solid-state Na–CO_2 batteries. (a) Discharge/charge curves of the batteries. (b) Raman spectra of the MWCNTs cathode at different states marked in (a).

After discharge, the stretching vibrational frequency at 1080 cm^{-1} appears, indicating the formation of Na_2CO_3.[15] This peak disappears after full charge, implying the reversible decomposition of Na_2CO_3.

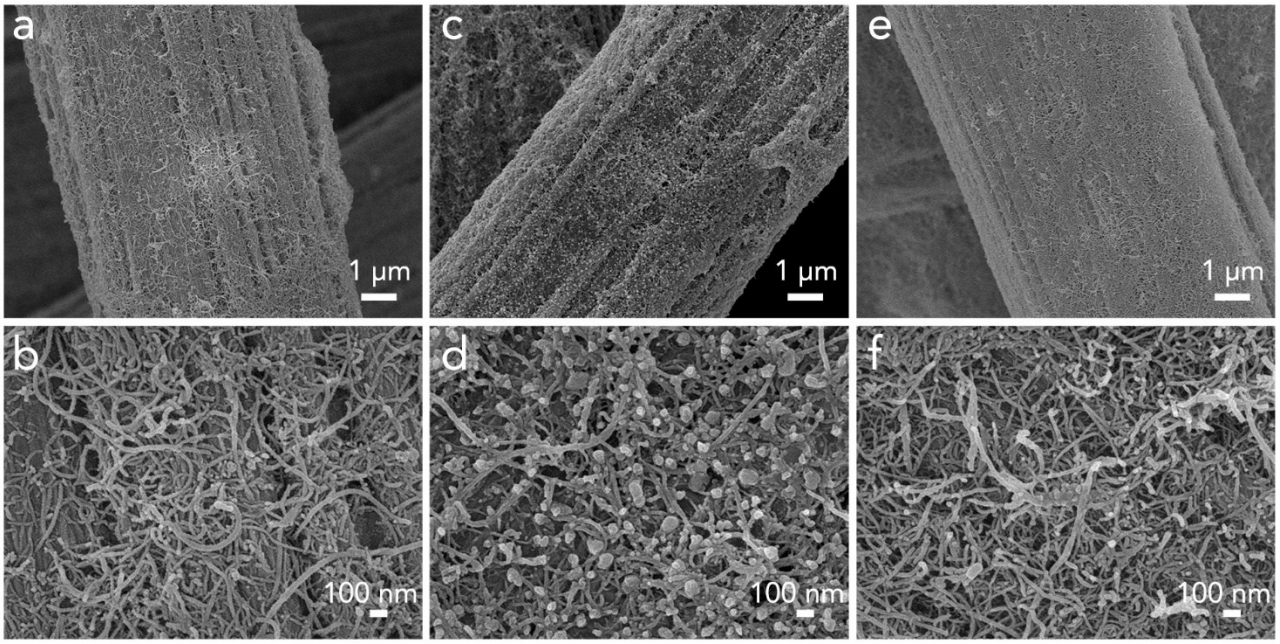

Figure S24. Morphology evolution (ex situ SEM) of the MWCNTs/carbon paper cathode in the all-solid-state Na–CO_2 batteries. (a,b) Initial state, (c,d) after discharge for 1000 mA h g^{-1}, and (e,f) after full charge.

After discharge, the generated products exist in the form of nanoparticles (50–100 nm) around the MWCNTs on the surface of carbon paper current collector. After charge, the nanoparticles can disappear reversibly.

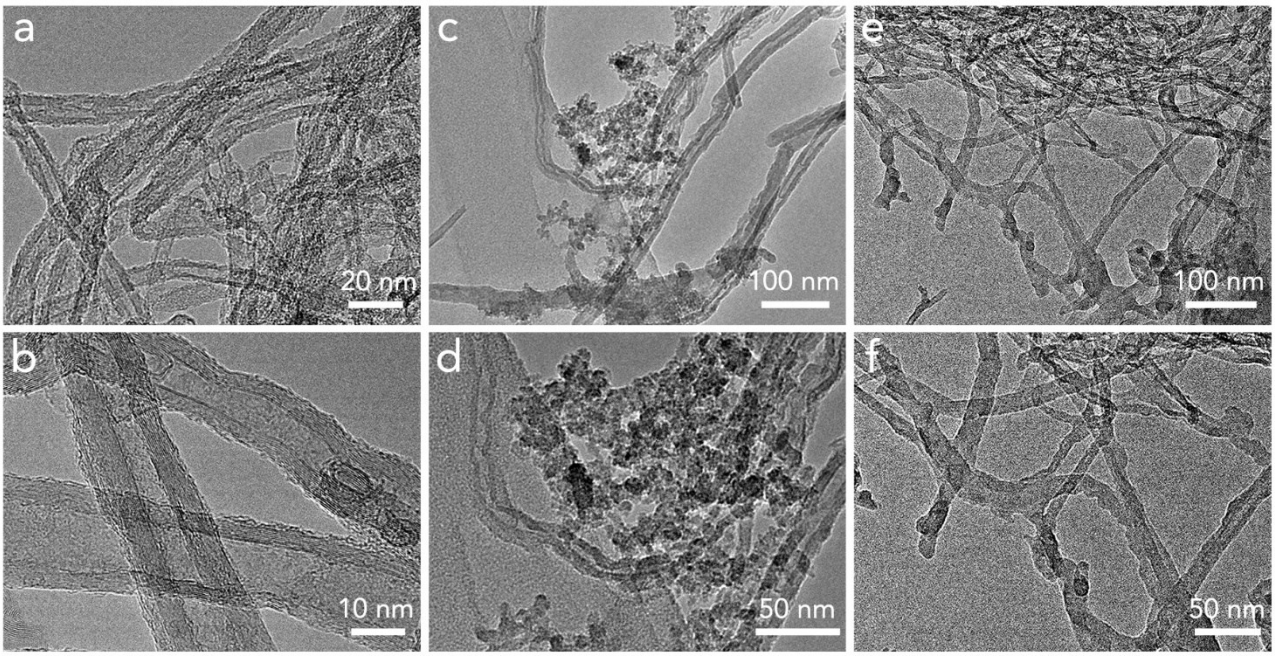

Figure S25. Ex situ TEM to reveal the reaction mechanism of the all-solid-state Na–CO_2 batteries. (a,b) Initial state, (c,d) after discharge for 1000 mA h g^{-1}, and (e,f) after full charge.

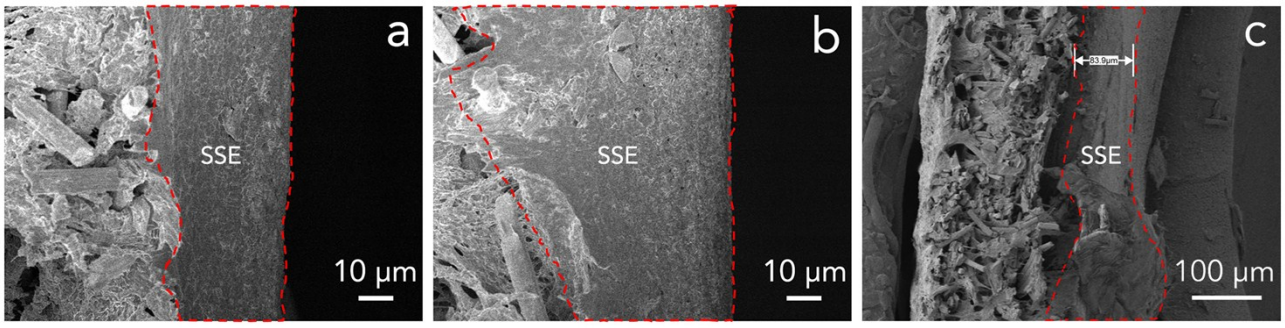

Figure S26. Cross-sectional SEM images of the integrated cathodes with different thickness of SN-based SSE. (a) 20–40 μm, (b) 50–70 μm, and (c) 80–100 μm.

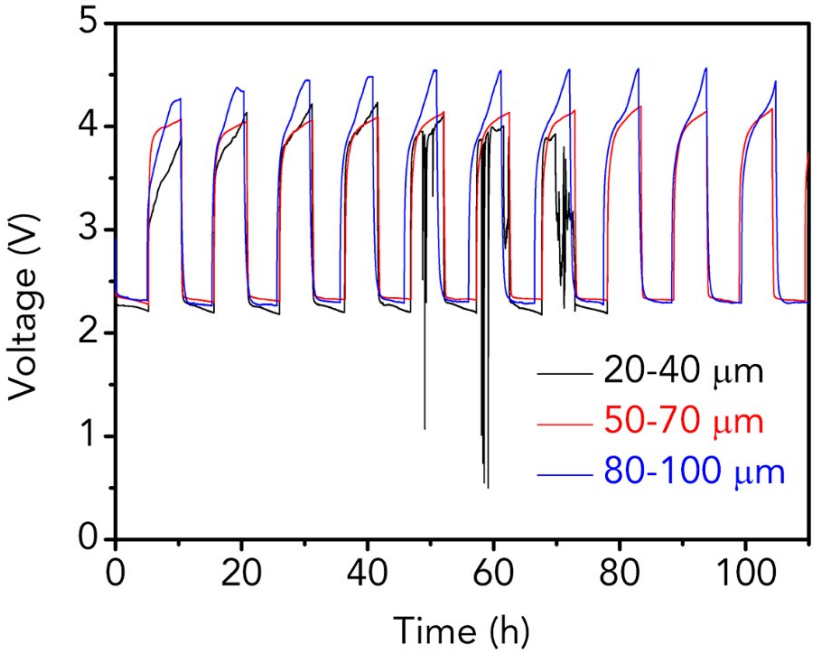

Figure S27. Voltage profiles of the all-solid-state Na–CO_2 batteries (modified Na as anode) with different SN-based SSE (thickness: 20–40, 50–70, and 80–100 μm) at 200 mA g^{-1}.

On one hand, when the thickness of SSE is too low (20–40 μm), the batteries tend to short circuit during discharge/charge processes. On the other hand, the overpotential of the batteries would be large if the SSE is too thick (80–100 μm). Thus, we select the SSE with moderate thickness (50–70 μm) to further study the electrochemical performance of the all-solid-state batteries.

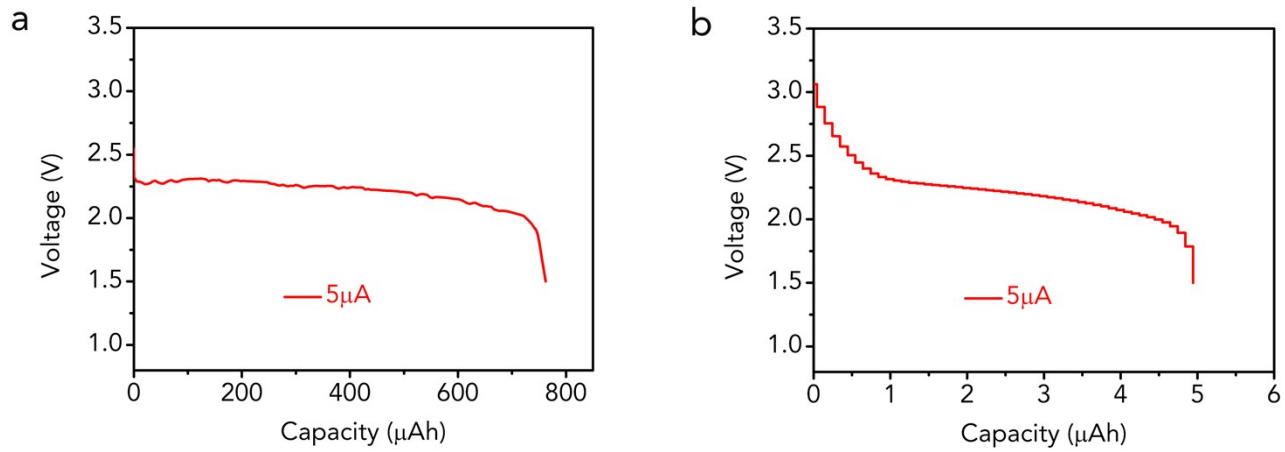

Figure S28. Full discharge curves of (a) MWCNTs/carbon paper cathode and (b) pure carbon paper current collector at 5 μA (50 mA g^{-1} based on the mass of MWCNTs).

The discharge capacities of MWCNTs/carbon paper cathode and pure carbon paper current collector at 5 μA are 763 and 5 μA h, respectively. The results demonstrate that the capacity derived from carbon paper current collector is negligible. Thus, the capacities and current densities of Na–CO_2 batteries in this work are calculated based on the mass of MWCNTs.

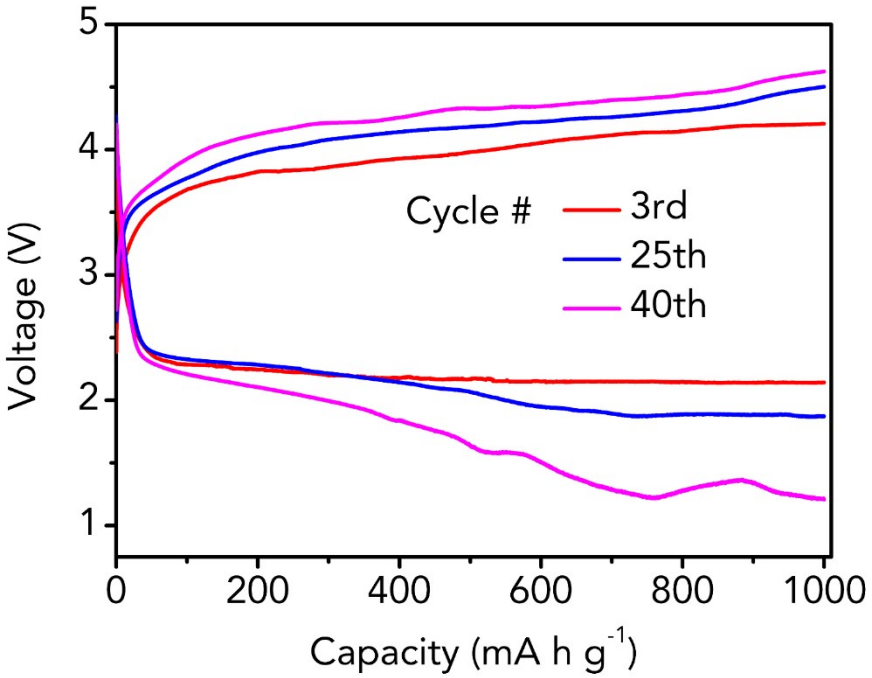

Figure S29. Charge/discharge curves of the all-solid-state Na–CO_2 batteries (pristine Na as anode) with a controlled specific capacity of 1000 mA h g^{-1} at 200 mA g^{-1} in different cycles.

Table S1. Comparison of electrochemical performance of this work versus other reported room-temperature metal–CO_2 batteries

Systems	Electrolyte /Cathodes	Cycle number /Gap (V) /Current (mA g^{-1})	Gap (V) /Rate (mA g^{-1})	Cycling/Maximal capacity (mA h g^{-1})	Ref.
Li–CO_2 batteries	Liquid /Graphene	20/1.4/50	1.5/100	1000/14000	16
	Liquid /CNT	29/1.6/50	1.7/100	1000/8300	17
	Liquid /Ru@Super P	70/1.5/200	1.6/300	1000/8000	18
	Liquid /Mo_2C/CNT	40/0.7/0.5	0.7/0.5	25/750	19
	Liquid /Mn_2(dobdc)	15/1.3/50	1.6/200	1000/18022	20
	Liquid /NiO-CNT	42/1.45/50	1.65/100	1000/9000	21
	Liquid /Cu-NG	50/0.8/200	1.4/400	1000/15000	22
	Liquid /Ir@CNFs	45/1.6/50	1.65/200	1000/22000	23
	Quasi-solid-state /CNTs	60/1.8/100	2.0/500	1000/8800	24
Na–CO_2 batteries	Liquid /t-MWCNT	200/0.6/1000	1.7/4000	2000/60000	25
	Quasi-solid-state /a-MWCNT	50/1.1/200	1.55/500	1000/-	26
	Liquid /CMO@CNF	75/1.47/100	2.19/500	500/8500	27
	All-solid-state /MWCNTs	100/1.54/200	2.08/500	1000/7624	This work
Al–CO_2 batteries	Liquid /NPG@Pd	30/0.091/333	0.091/333	333/3330	28

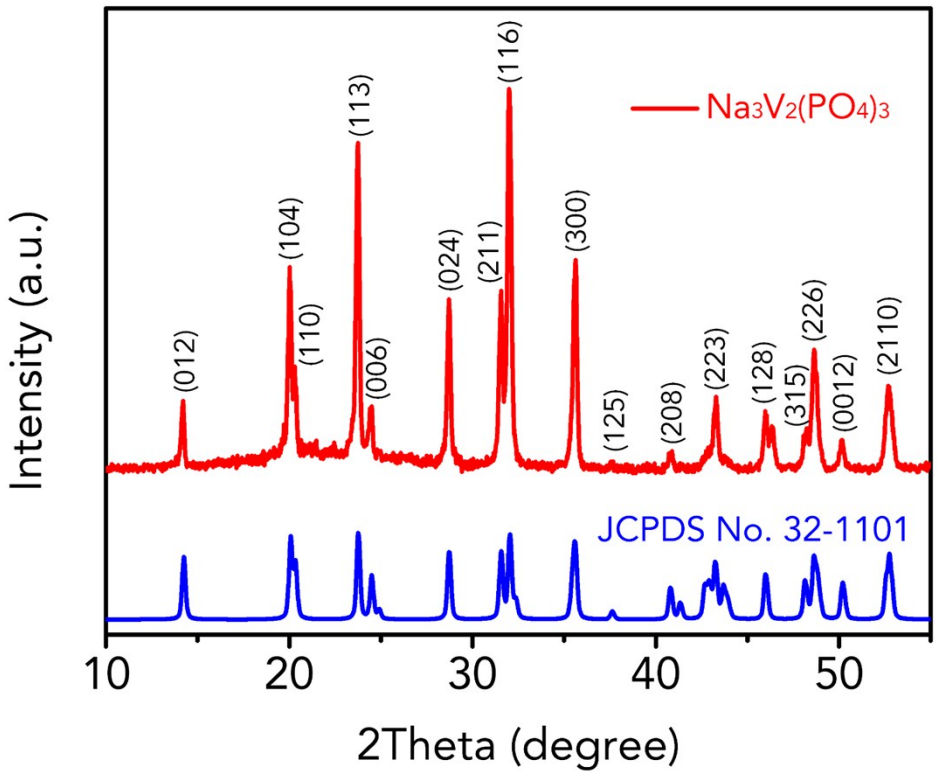

Figure S30. XRD pattern of the synthesized $Na_3V_2(PO_4)_3$ sample.

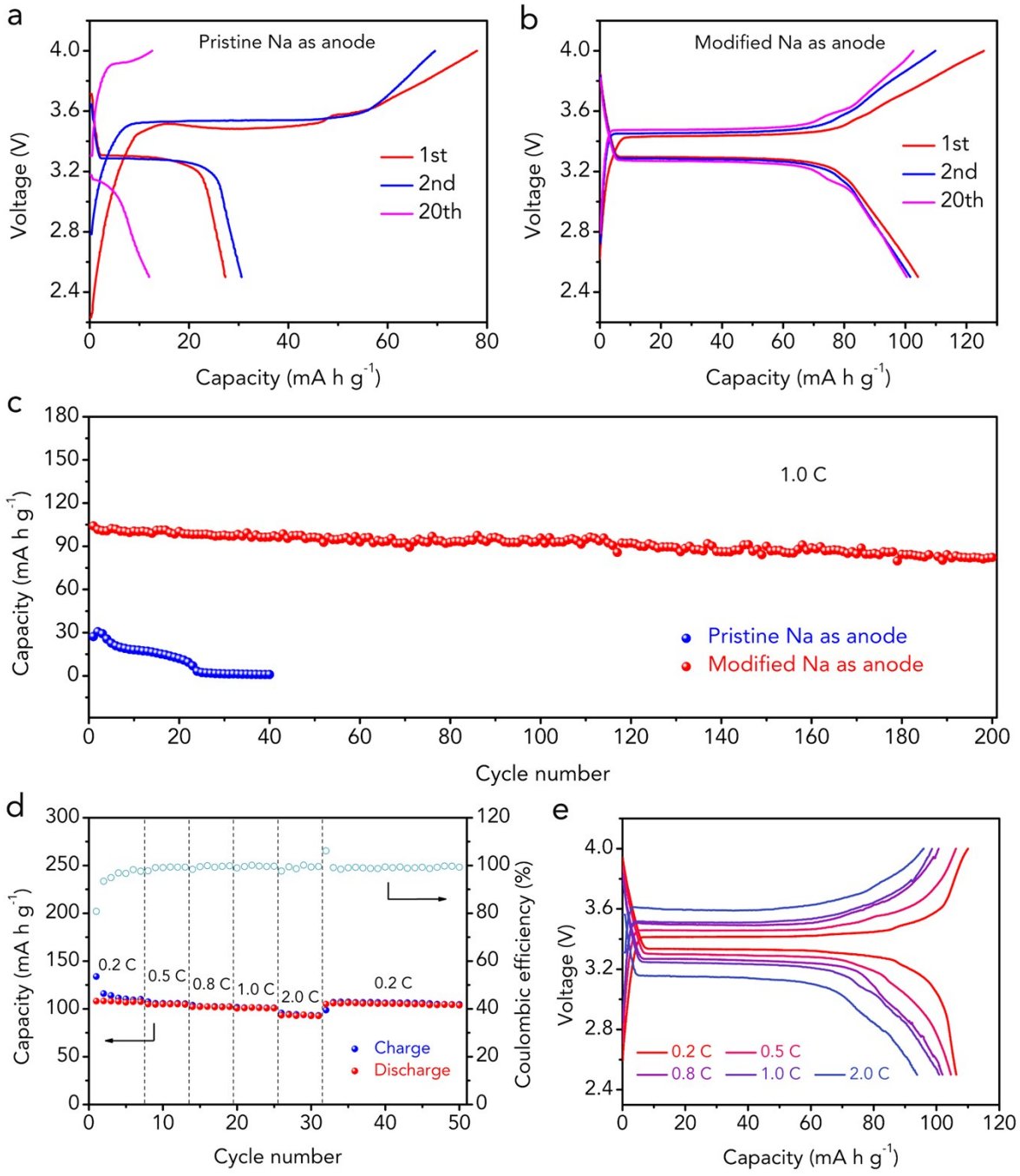

Figure S31. Electrochemical performance of the all-solid-sate Na|$Na_3V_2(PO_4)_3$ batteries in the voltage range of 2.5–4.0 V. Discharge/charge curves of the batteries with (a) pristine Na and (b) modified Na as anode at 1.0 C (118 mA g^{-1}). (c) Cycling performance of the batteries with pristine Na and modified Na as anode at 1.0 C. (d) Rate capability/Coulombic efficiency and (e) discharge/charge profiles of

the batteries with modified Na as anode at different rates (0.2, 0.5, 0.8, 1.0, and 2.0 C).

As shown in Figure S31a, the discharge capacities of the batteries with pristine Na as anode are only 28, 31, and 12 mA h g^{-1} in the 1st, 2nd, and 20th cycle, respectively. Moreover, the cycling stability of the batteries is rather poor (Figure S31b). The inferior electrochemical performance of the batteries with pristine Na as anode can be attributed to the serious side reactions between Na and SN-based SSE, leading to continuously increased interfacial resistance and unfavorable Na^+ ions transfer.

In contrast, the batteries with modified Na as anode exhibit high discharge capacities of 104, 102, 101, and 83 mA h g^{-1} in the 1st, 2nd, 20th, and 200th cycle, respectively (Figure S31b), corresponding to a good capacity retention of 80% after 200 cycles (Figure S31c). Moreover, the batteries with modified Na as anode show superior rate performance (Figure S31d,e). The discharge capacity could still maintain 94 mA h g^{-1} at a high rate of 2.0 C. These results indicate that the compatible Na anode/succinonitrile-based electrolyte interface could also be extended to other all-solid-state Na battery systems such as the Na|$Na_3V_2(PO_4)_3$ batteries.

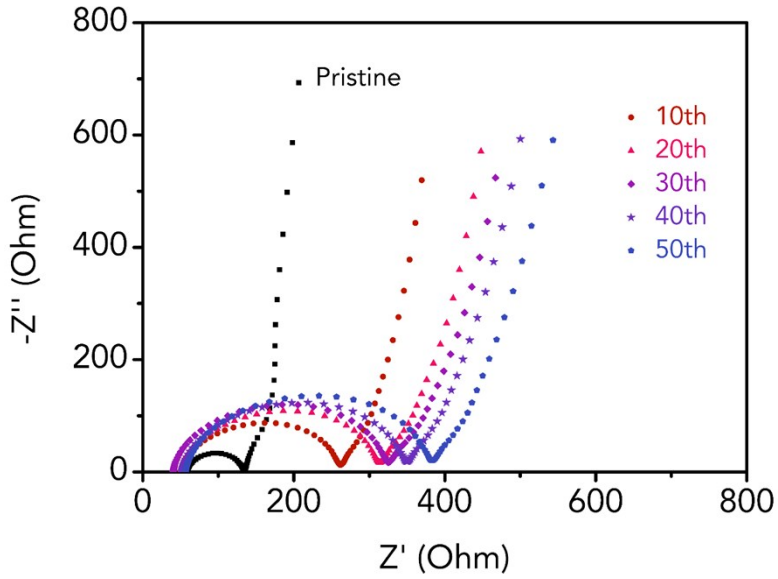

Figure S32. EIS plots of the all-solid-sate $Na_3V_2(PO_4)_3|Na_3V_2(PO_4)_3$ symmetric batteries at different states: pristine, after 10^{th}, 20^{th}, 30^{th}, 40^{th}, and 50^{th} cycles. The symmetric batteries cycled at 1.0 C in the voltage range of 1.0–3.0 V.

According to the EIS plots, we found that charge transfer resistance of the all-solid-sate $Na_3V_2(PO_4)_3|Na_3V_2(PO_4)_3$ symmetric batteries gradually increase during cycles, indicating that there may be slight side reactions between $Na_3V_2(PO_4)_3$ and SSE.

References

(1) Koch, W.; Holthausen, M. C. *A Chemist's Guide to Density Functional Theory*, 2nd ed.; Wiley-VCH: Weinheim, 2015.

(2) Parr, R. G.; Yang, W. *Density-Functional Theory of Atoms and Molecules*; Oxford University Press: New York, 1989.

(3) Frisch, M. J.; Trucks, G. W.; Schlegel, H. B.; Scuseria, G. E.; Robb, M. A.; Cheeseman, J. R.; Scalmani, G.; Barone, V.; Mennucci, B.; Petersson, G. A.; Nakatsuji, H.; Caricato, M.; Li, X.; Hratchian, H. P.; Izmaylov, A. F.; Bloino, J.; Zheng, G.; Sonnenberg, J. L.; Hada, M.; Ehara, M.; Toyota, K.; Fukuda, R.; Hasegawa, J.; Ishida, M.; Nakajima, T.; Honda, Y.; Kitao, O.; Nakai, H.; Vreven, T.; Montgomery Jr., J. A.; Peralta, J. E.; Ogliaro, F.; Bearpark, M.; Heyd, J. J.; Brothers, E.; Kudin, K. N.; Staroverov, V. N.; Kobayashi, R.; Normand, J.; Raghavachari, K.; Rendell, A.; Burant, J. C.; Iyengar, S. S.; Tomasi, J.; Cossi, M.; Rega, N.; Millam, J. M.; Klene, M.; Knox, J. E.; Cross, J. B.; Bakken, V.; Adamo, C.; Jaramillo, J.; Gomperts, R.; Stratmann, R. E.; Yazyev, O.; Austin, A. J.; Cammi, R.; Pomelli, C.; Ochterski, J. W.; Martin, R. L.; Morokuma, K.; Zakrzewski, V. G.; Voth, G. A.; Salvador, P.; Dannenberg, J. J.; Dapprich, S.; Daniels, A. D.; Farkas, Ö.; Foresman, J. B.; Ortiz, J. V.; Cioslowski, J.; Fox, D. J. *Gaussian 09*, revision A.01; Gaussian, Inc.: Wallingford, CT, 2009.

(4) Perdew, J. P.; Burke, K.; Ernzerhof, M. Generalized Gradient Approximation Made Simple. *Phys. Rev. Lett.* **1996**, *77*, 3865−3868.

(5) Kresse, G.; Hafner, J. Ab Initio Molecular Dynamics for Open-Shell Transition Metals. *Phys. Rev. B* **1993**, *48*, 13115–13118.

(6) Kresse, G.; Furthmüller, J. Efficient Iterative Schemes for *Ab Initio* Total-Energy Calculations Using a Plane-Wave Basis Set. *Phys. Rev. B: Condens. Matter Mater. Phys.* **1996**, *54*,

11169−11186.

(7) Kresse, G.; Furthmüller, J. Efficiency of Ab-Initio Total Energy Calculations for Metals and Semiconductors Using a Plane-wave Basis Set. *Comput. Mater. Sci.* **1996**, *6*, 15–50.

(8) Blöchl, P. E. Projector Augmented-Wave Method. *Phys. Rev. B* **1994**, *50*, 17953–17979.

(9) Kresse, G.; Joubert, D. From Ultrasoft Pseudopotentials to the Projector Augmented-Wave Method. *Phys. Rev. B* **1999**, *59*, 1758–1775.

(10) Monkhorst, H. J.; Pack, J. D. Special Points for Brillouin-Zone Integrations. *Phys. Rev. B* **1976**, *13*, 5188–5192.

(11) Lu, Y.; Zhao, Q.; Miao, L.; Tao, Z.; Niu, Z.; Chen, J. Flexible and Free-Standing Organic/Carbon Nanotubes Hybrid Films as Cathode for Rechargeable Lithium-Ion Batteries. *J. Phys. Chem. C* **2017**, *121*, 14498−14506.

(12) Zhang, X.; Wang, X.; Liu, S.; Tao, Z.; Chen, J. A Novel PMA/PEG-Based Composite Polymer Electrolyte for All-Solid-State Sodium Ion Batteries. *Nano Res.* **2018**, *11*, 6244–6251.

(13) Zhao, C.-Z.; Zhang, X.-Q.; Cheng, X.-B.; Zhang, R.; Xu, R.; Chen, P.-Y.; Peng, H.-J.; Huang, J.-Q.; Zhang, Q. An Anion-Immobilized Composite Electrolyte for Dendrite-Free Lithium Metal Anodes. *Proc. Natl. Acad. Sci. U. S. A.* **2017**, *114*, 11069–11074.

(14) Wöhrle, D.; Knothe, G. *J. Polym. Sci., Part A: Polym. Chem.* **1988**, *26*, 2435–2447.

(15) Brooker, M. H.; Bates, J. B. Raman and Infrared Spectral Studies of Anhydrous Li_2CO_3 and Na_2CO_3. *J. Chem. Phys.* **1971**, *54*, 4788–4796.

(16) Zhang, Z.; Zhang, Q.; Chen, Y.; Bao, J.; Zhou, X.; Xie, Z.; Wei, J.; Zhou, Z. The First Introduction of Graphene to Rechargeable Li-CO_2 Batteries. *Angew. Chem. Int. Ed.* **2015**, *54*, 6550–6553.

(17) Zhang, X.; Zhang, Q.; Zhang, Z.; Chen, Y.; Xie, Z.; Wei, J.; Zhou, Z. Rechargeable Li–CO_2

Batteries with Carbon Nanotubes as Air Cathodes. *Chem. Commun.* **2015**, *51*, 14636−14639.

(18) Yang, S.; Qiao, Y.; He, P.; Liu, Y.; Cheng, Z.; Zhu, J.-j.; Zhou, H. A Reversible Lithium–CO_2 Battery with Ru Nanoparticles as a Cathode Catalyst. *Energy Environ. Sci.* **2017**, *10*, 972−978.

(19) Hou, Y.; Wang, J.; Liu, L.; Liu, Y.; Chou, S.; Shi, D.; Liu, H.; Wu, Y.; Zhang, W.; Chen, J. Mo_2C/CNT: An Efficient Catalyst for Rechargeable Li-CO_2 Batteries. *Adv. Funct. Mater.* **2017**, *27*, 1700564.

(20) Li, S.; Dong, Y.; Zhou, J.; Liu, Y.; Wang, J.; Gao, X.; Han, Y.; Qi, P.; Wang, B. Carbon Dioxide in the Cage: Manganese Metal–Organic Frameworks for High Performance CO_2 Electrodes in Li-CO_2 Batteries. *Energy Environ. Sci.* **2018**, *11*, 1318−1325.

(21) Zhang, X.; Wang, C.; Li, H.; Wang, X.-G.; Chen, Y.-N.; Xie, Z.; Zhou, Z. High Performance Li–CO_2 Batteries with NiO-CNT Cathodes. *J. Mater. Chem. A* **2018**, *6*, 2792−2796.

(22) Zhang, Z.; Zhang, Z.; Liu, P.; Xie, Y.; Cao, K.; Zhou, Z. Identification of Cathode Stability in Li–CO_2 Batteries with Cu Nanoparticles Highly Dispersed on N-Doped Graphene. *J. Mater. Chem. A* **2018**, *6*, 3218−3223.

(23) Wang, C.; Zhang, Q.; Zhang, X.; Wang, X.-G.; Xie, Z.; Zhou, Z. Fabricating Ir/C Nanofiber Networks as Free-Standing Air Cathodes for Rechargeable Li–CO_2 Batteries. *Small* **2018**, *14*, 1800641.

(24) Li, C.; Guo, Z.; Yang, B.; Liu, Y.; Wang, Y.; Xia, Y. A Rechargeable Li–CO_2 Battery with Gel Polymer Electrolyte. *Angew. Chem. Int. Ed.* **2017**, *56*, 9126–9130.

(25) Hu, X.; Sun, J.; Li, Z.; Zhao, Q.; Chen, C.; Chen, J. Rechargeable Room-Temperature Na–CO_2 Batteries. *Angew. Chem. Int. Ed.* **2016**, *55*, 6482−6486.

(26) Hu, X.; Li, Z.; Zhao, Y.; Sun, J.; Zhao, Q.; Wang, J.; Tao, Z.; Chen, J. Quasi–Solid State Rechargeable Na–CO_2 Batteries with Reduced Graphene Oxide Na Anodes. *Sci. Adv.* **2017**, *3*,

e1602396.

(27) Fang, C.; Luo, J.; Jin, C.; Yuan, H.; Sheng, O.; Huang, H.; Gan, Y.; Xia, Y.; Liang, C.; Zhang, J.; Zhang, W.; Tao, X. Enhancing Catalyzed Decomposition of Na_2CO_3 with Co_2MnO_x Nanowire-Decorated Carbon Fibers for Advanced Na–CO_2 Batteries. *ACS Appl. Mater. Interfaces* **2018**, *10*, 17240−17248.

(28) Ma, W.; Liu, X.; Li, C.; Yin, H.; Xi, W.; Liu, R.; He, G.; Zhao, X.; Luo, J.; Ding, Y. Rechargeable Al–CO_2 Batteries for Reversible Utilization of CO_2. *Adv. Mater.* **2018**, *30*, 1801152.